Improving cosmic-ray tomography of shipping containers with secondary particles

Maximilian Pérez Prada*, Maurice Stephan, Sarah Barnes
Institute for the Protection of Maritime Infrastructures
German Aerospace Center (DLR)
Fischkai 1, 27572 Bremerhaven, Germany

***Abstract*—Cosmic-ray tomography has emerged as a new imaging method, with applications in a variety of fields, including safety and security. The concept of this technique is most commonly based on the measurement of the transmission or scattering of muons from cosmic-ray air showers within the volume of interest. However, during the interaction of these muons and other air shower particles with the examined objects, secondary particles are produced, which can also be utilized to gain information about the material properties of target objects. This work provides improvements to a reconstruction approach based solely on secondary particles in the context of shipping container scanning. The focus of the work is the derivation of correction factors for reconstructed object properties to allow a consistent comparison of objects anywhere within the volume. This is required due to position dependent effects on the reconstructed density and position of objects resulting from different detector sensitivities to particular secondary particles.**

***Index Terms*—cosmic-ray, tomography, secondary particle, shipping container**

I. Introduction

In recent years, cosmic-ray tomography (CRT) has emerged as a new concept in the field of non-destructive imaging, with applications in a wide range of fields, like analyzing the interior of volcanoes or pyramids, as well as scanning shipping containers for contraband in the port [1-8]. When high-energy cosmic-rays interact with the nuclei of atoms in earth's atmosphere, a cascade of energetic particles forms reaching down to earth's surface. This cascade is called an air shower and at sea level consists mainly of muons, photons and neutrinos, in smaller fractions also protons, neutrons, electrons and pions [9-12]. Muons from air showers are an ideal and natural source of radiation, which can be used for imaging purposes, as they provide a high material penetration depth due to their high energy.

CRT is mainly based on two methods: Muon Scattering Tomography (MST) and Muon Radiography (MR). MST utilizes the interaction of muons with the atoms of the examined material through Coulomb scattering. The scattering angle is dependent on specific material properties, such as the atomic number and the density. Hence, measuring the deflection of the muon trajectory allows for the reconstruction of objects and their properties in the volume of interest [13, 14]. MR is based on the muon absorption rate, which is also proportional on the density of the material [15, 16].

Air shower particles passing through matter undergo additional physical interactions like bremsstrahlung or muon capture, which result in energy loss and the production of additional, so-called secondary particles, mainly photons, electrons and neutrons. The kinematics and production rate of these particles depends on the material properties [17-25]. This creates a complementary source of information relating to the properties of the examined volume compared with measurements obtained from MST or MR. The approach of utilizing the secondary particle information has been validated in theory and experiment, mainly by measuring the secondary particles in coincidence with incoming air shower muons [26-30]. Previous work by the authors showed the feasibility of a stand-alone technique for the scanning of containers based on simulation studies, solely relying on the measurement on secondary particles including optimal and realistic detection conditions [31, 32].

This work builds upon the methods presented in [32], with the aim of providing correction maps for the reconstructed density and position of the examined objects inside the container. These corrections are needed, as the location of the target object in the shipping container impacts the reconstructed attributes of the object, such as its reconstructed position and the material density. This effect is a consequence of the reconstruction method introduced in [31, 32]. For each detector above, below or to the side of the shipping container, as well as for each type of secondary particle and for different particle energies, a single measurement is established. By subsequently combining individual detector measurements and utilizing their different sensitivities to the secondary particle origin and type, a successful discrimination between materials is possible. However, as the distance from the target object to each detector varies depending on its location within the container, the sensitivity of each measurement varies accordingly. This results in the reconstruction of biased object attributes based on the original position of the target object, leading to inconsistent comparison and discrimination between different objects and materials. Hence, the combination or comparison of the results from this approach based on secondary particles with the measurements from MST or MR additionally require a correction of the reconstructed properties.

This research was funded by the SilentBorder project under the grant agreement ID 101021812 of the European Union's Horizon 2020 research and innovation program.

* Email address for correspondence: m.perezprada@dlr.de

II. Simulation setup

The analysis is carried out using the GEANT4 Monte Carlo simulation toolkit [33, 34] for all interactions of particles with matter. The type and kinematics of all air shower particles are derived from the precomputed parametrized look-up tables in the Cosmic-ray Shower Library (CRY) [12] at sea level. The scanning time is set to 30 minutes, which is equivalent to around 100 million air showers.

A 1 m^3 cube made out of lead or water is used as the target object and located in the middle of a simplified container made out of stainless steel. The center of the container is also set as the origin of the coordinate system, with the x-axis along the width, the y-axis along the length and the z-axis along the height of the container. A set of three 50 mm thick detector layers spaced by 10 cm is placed above, below, to the left and to the right of the container, as visualized in Figure 1. The material of each detection layer is set to a Vinyltoluene based plastic scintillator to mimic a realistic detection material. The detectors form an inspection volume of 3.5 m × 7.0 m × 3.5 m.

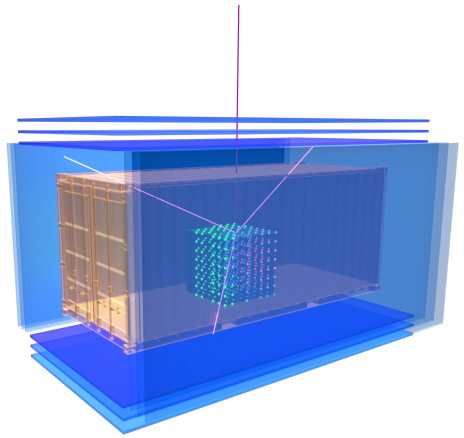

Fig. 1. Visualization of the detector and container setup. The blue planes indicate the detector layers, the colored dots represent the reconstructed density of the generic object located inside the container. The purple line represents the trajectory of an air shower particle, the pink lines the path of produced secondary particles.

The particle energy, the particle type, as well as the point, where the particle hit the scintillator, are directly inferred from the GEANT4 simulation at each detector layer, hence no readout from the scintillator material and no particle identification is emulated. Only particles originating from the interior of the examined volume and interacting with all three scintillator layers of one of the four detector sets are utilized. The final kinematics of each particle are derived with a least squares based fit over the three points of interaction with the detection layers. For simplicity, the detection efficiency is set to 100 % and perfect spatial resolution is assumed. This can be justified, as [32] shows that the impact of spatial resolution on the final reconstruction is reasonably small (< 15 %) and applying a non-perfect detection efficiency is equivalent to a proportional reduction in scanning time. In reality, the detection efficiencies vary between the secondary particle types and over the energy spectrum. However as shown in [32], the measurement of the particle type with the lowest detection efficiency has the biggest impact on the results due to the role of the different measurements in the reconstruction method discussed in Section III.

III. Reconstruction method

The reconstruction of the voxelized volume, the so-called voxel map, containing the container and its content is based on the back-tracing of each detected secondary particle (photon, neutron, electron) on a linear path. Starting from the detected position at the innermost scintillator layer, each voxel crossed by the particle trajectory gets marked. The number of crossings per voxel is representative of certain material properties, primarily the density and atomic number. The final score value per voxel is referred to as the density score s_{voxel}. To remove the secondary particle background produced from the container and detector material, the voxel map of an empty container is measured with 1 billion air shower events and subtracted from every test scenario.

Twelve voxel maps corresponding to detector specific measurements defined in Table I and denoted $M1$-$M10$ are created. Each voxel map corresponds to a different detector position (upper detector, sidewise detector, lower detector), type of secondary particle (photon, neutron, electron) and particle energy regime. The differentiation by particle energy allows the discrimination between the production and absorption of secondary and air shower particles during the interactions with the objects inside the container resulting in an improved determination of the material. More details on the measurement scheme and its foundation can be found in [31, 32].

TABLE I
DEFINITION OF THE MEASUREMENTS DEFINED BY THE PARTICLE TYPE, THE PARTICLE ENERGY AND THE DETECTOR POSITION. $M2.1$ AND $M2.2$, AS WELL AS $M5.1$ AND $M5.2$ ARE MUTUALLY EXCLUSIVE.

	Photons	**Neutrons**	**Electrons**
Upper detector: Production	$M1^{\alpha}$, $M2.1^{\beta}$	$M3$	–
Upper detector: Absorption	$M2.2^{\beta}$	–	–
Sidewise detector: Production	$M4^{\alpha}$, $M5.1^{\beta}$	$M6$	–
Sidewise detector: Absorption	$M5.2^{\beta}$	–	–
Lower detector: Production	–	$M8^{\gamma}$	–
Lower detector: Absorption	$M7$	$M9^{\delta}$	$M10$

$^{\alpha} > 400$ keV, $^{\beta} < 400$ keV, $^{\gamma} < 3$ MeV, $^{\delta} > 3$ MeV

For each material, a unique set of the twelve measurements is combined by summing the density scores voxel by voxel utilizing the different kinematics of secondary particles originating from different materials embodied in each map. The voxel maps included in the combination are based on a manually derived statistical significance of each measurement to avoid

the inclusion of background noise. During the combination, a manually chosen minimum density score threshold t_{min} is applied for each voxel map with respect to the maximum density score s_{max} in the particular map, acting as a filter to further reduce background noise:

$$s_{voxel} > s_{max} \cdot t_{min} \tag{1}$$

The list of measurements and density score thresholds used to reconstruct the water and lead cube are given in Tables II and III. For the reconstruction of the water cube, $M1$ and $M2.1$, as well as $M4$ and $M5.1$ are merged into one measurement to enhance its statistical significance for the combination.

TABLE II
MEASUREMENTS AND DENSITY SCORE THRESHOLDS USED IN THE RECONSTRUCTION OF THE WATER CUBE.

	Photons	**Neutrons**	**Electrons**
Upper detector: Production	20 %	–	–
Upper detector: Absorption	–	–	–
Sidewise detector: Production	30 %	–	–
Sidewise detector: Absorption	–	–	–
Lower detector: Production	–	–	–
Lower detector: Absorption	30 %	40 %	40 %

TABLE III
MEASUREMENTS AND DENSITY SCORE THRESHOLDS USED IN THE RECONSTRUCTION OF THE LEAD CUBE.

	Photons	**Neutrons**	**Electrons**
Upper detector: Production	15 % $^{\alpha}$, – $^{\beta}$	15 %	–
Upper detector: Absorption	–	–	–
Sidewise detector: Production	25 % $^{\alpha}$, – $^{\beta}$	25 %	–
Sidewise detector: Absorption	–	–	–
Lower detector: Production	–	–	–
Lower detector: Absorption	40 %	40 %	50 %

$^{\alpha} > 400$ keV, $^{\beta} < 400$ keV

In the last step of the reconstruction, a clustering method is applied to the voxel map to segment the target object over the background. The voxel with the combined highest density score is used as the seed for the clustering algorithm. Afterwards, the method loops over all surrounding voxel and incorporates them into the cluster in case of a density score of minimum 80 % of the mean cluster density score.

IV. CORRECTION MAPS

The reconstructed density score and position of the target object show a dependency on the original location of the reconstructed object within the container. The variation of the density score results from the changing detector acceptances of each measurement as the score is directly proportional to the number of secondary particles associated with the reconstructed object. If, for instance, the target object is located closer to the doors in the front or back of the container (see Figure 1), the fraction of secondary particles produced towards the direction without detector coverage increases resulting in a lower overall density score towards the extreme values in the direction of the y-axis. This effect is shown in Figures 2, in which a lead cube is positioned in the back, center and front of the container.

The variation of the density score is also dependent on the selection of the detector positions used in the combination of the measurements. Most of the secondary particles are produced in the top volume of the target object, hence the upper detector is the most sensitive detection position and therefore the dominant measurement in the combination. As the cube moves closer to the bottom of the container, the relevance of the lower detector position should increase. However, in general a lower number of secondary particles reach the lower detector due to self-shielding effects reducing the significance of this measurement in the combination. In addition, the absorption measurement in the lower detector position is also less relevant than the measurement from the upper detector position, as it is only sensitive to the shadow of the entire object and not to secondary particles produced in a certain volume resulting in a large spatial resolution of this measurement along the z-axis. Hence, the reconstructed density score decreases with growing distance to the upper detector position, as the chance of a secondary particle getting absorbed in the air or other intermediate material before reaching the detector increases.

The reconstructed position of the cube gets impacted in a similar way. As the upper volume of the object produces the majority of secondary particles, the reconstructed location of the object center is shifted towards the upward direction of the z-axis compared with the true location. The further away the cube is located from the upper detector position, which is the most relevant measurement, the more significant this shift appears, as the spatial uncertainty of this measurement along the z-axis is rising with increasing distance to the detector. As described before, the measurements in the lower detector position are not significant enough to counteract this effect. Hence, the shift of the reconstructed position of the object compared to the original location increases the closer the cube is located towards the bottom of the container.

These and other similar systematic effects on the reconstructed properties due to the position of the object create the problem of potentially ambiguous results. Especially the variation in the density score appears to be a critical issue, as this could lead to a systematic bias in the material classification. This presents a potential problem when considering a combination with results from MST or MR, as well as the application of machine learning methods for automatic material segmentation and classification. Hence, correction maps for the reconstructed density score and object position

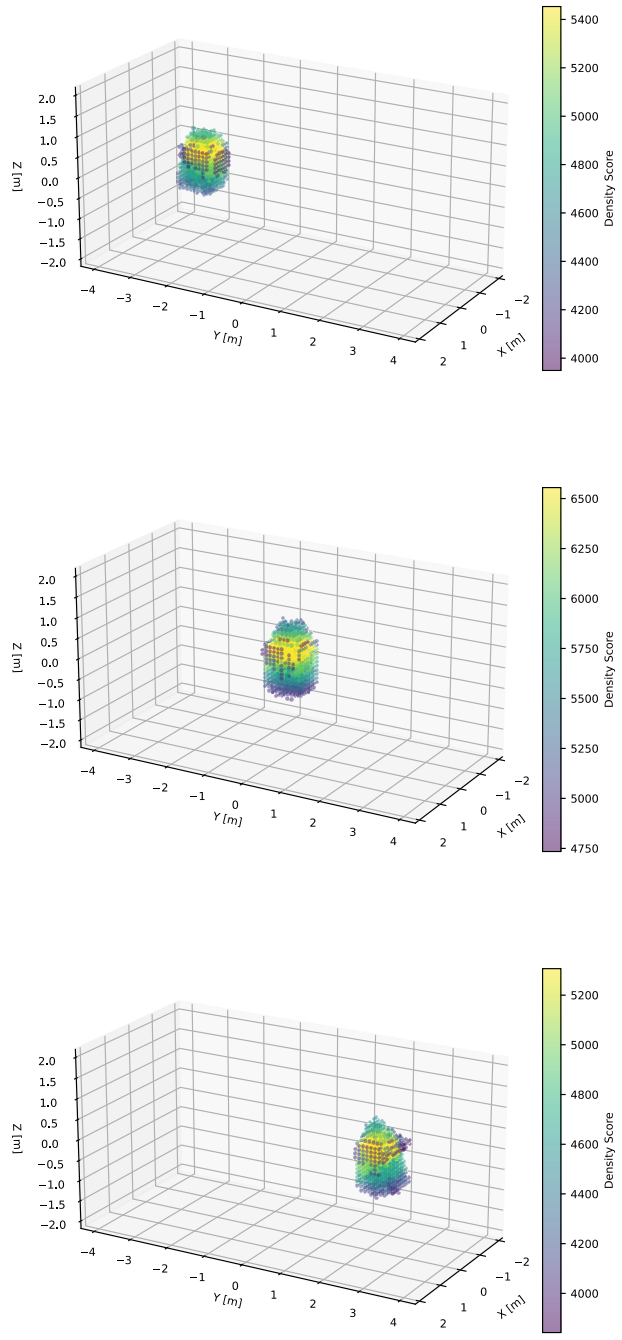

Fig. 2. Reconstruction of a 1 m^3 lead cube located at various positions inside the container: (top) at the back, (middle) at the center, (bottom) at the front.

need to be measured and validated. As the combination of the measurements is material dependent, two separate correction maps, one for the lead cube and one for the water cube, are required. Since this work serves as a proof-of-principle, only this small subset of two materials is used.

The corrections for both properties are measured at 33 different positions throughout the volume inside the container starting with the center location. For each axis of the container, the minimum and maximum position, as well as the midpoints between the center and the minimum/maximum are selected. Furthermore, all positions, where at least two directions are at their minimum/maximum (e.g. the corners in the container), are also used to measure the adjustments. For the density score correction, the score value reconstructed at the center position is set as the true value, the so-called benchmark, as the density score can not be retrieved directly from simulation. For all other 32 positions the correction factor is measured as the ratio of the score at each location over the benchmark. The corrections for the reconstructed position are based on the positional shift between the reconstructed and the true simulated position of the cube, which is set as the benchmark in this case. With these measurements, a correction map with five bins for each axis based on the measurement positions is created for each reconstructed object property. The intermediate bins, for which no dedicated measurement was performed, are filled with manually interpolated corrections as the simulation of all 125 scenarios was not feasible within a reasonable time frame. For simplicity, the interpolation is based on symmetric arguments and the assumption of a linear behavior of the corrections between the measurement positions.

V. Results

The corrections are validated in two closure tests: First, a self-closure test is performed using all positions, which were part of the derivation of the correction maps. This is followed by a validation test based on five arbitrary positions as shown in Table IV, which are not part of the self-closure test.

TABLE IV
Coordinates of the arbitrary selected positions used for the validation closure test.

	X-Coordinate	Y-Coordinate	Z-Coordinate
Position 1	0.44 m	–0.13 m	–0.36 m
Position 2	0.25 m	0.78 m	–0.20 m
Position 3	0.06 m	–0.49 m	–0.15 m
Position 4	0.00 m	1.78 m	0.37 m
Position 5	–0.41 m	1.21 m	0.17 m

To asses the performance of the closure tests for the density score, the standard deviation σ_D of the relative differences between the density score at the closure test positions d_i and the benchmark score d_B is used as the closure metric:

$$\sigma_D = \sqrt{\frac{1}{N}\sum_{i=1}^{N}(\frac{d_i}{d_B} - 1)^2} \tag{2}$$

Similarly, the standard deviation σ_P of the absolute difference between the reconstructed object position p_i and the benchmark position p_B is established as the closure metric for the cube position correction map:

$$\sigma_P = \sqrt{\frac{1}{N}\sum_{i=1}^{N}(p_i - p_B)^2} \tag{3}$$

The results of the self-closure test are shown in Table V, with the outcomes of the validation test in Table VI. Overall, the application of the correction maps shows a significant improvement of the metrics for both properties and materials, varying between around 65-90 % for the self-closure and around 35-80 % for the validation test. The results after the adjustments from the self-closure, as well as the validation test are both at a similar level supporting the general idea and method introduced in this work. The self-closure metrics before the correction are significantly worse than the ones in the validation set. This can be explained by the extremeness of the positions used in the self-closure compared to the set of random points in the validation test, as the biggest bias is usually seen at the maximum/minimum positions inside the container. This is especially the case for the density score, as the position at the front/back of the container comes with the biggest correction due to the acceptance loss, which was already discussed in the previous section (see Figure 2). The statistical precision of the results for the water cube is lower than the statistical precision of the results for the lead cube as it is reconstructed from a lower number of secondary particles due to the lower density of the material. This can be seen in the slightly worse performance of the corrected validation test results, where statistical variations are more prone to be visible than in the self-closure results due to the selection of arbitrary points.

TABLE V
RESULTS OF THE SELF-CLOSURE TEST FOR THE LEAD AND WATER CUBE.

	LEAD		**WATER**	
	$\boldsymbol{\sigma_D}$	$\boldsymbol{\sigma_P}$	$\boldsymbol{\sigma_D}$	$\boldsymbol{\sigma_P}$
Before correction	15.5 %	0.13 m	13.8 %	0.11 m
After correction	1.3 %	0.02 m	1.5 %	0.04 m

TABLE VI
RESULTS OF THE VALIDATION TEST FOR THE LEAD AND WATER CUBE.

	LEAD		**WATER**	
	$\boldsymbol{\sigma_D}$	$\boldsymbol{\sigma_P}$	$\boldsymbol{\sigma_D}$	$\boldsymbol{\sigma_P}$
Before correction	3.7 %	0.18 m	3.0 %	0.12 m
After correction	1.3 %	0.04 m	1.9 %	0.07 m

Both materials shows similar values for the considered metrics before the correction supporting the hypothesis that the biases are likely a result of the reconstruction methodology. However, as the values are slightly higher for the lead cube compared to the water cube, the composition of the target object seems to also play a role. This is also shown in Table VII, which contains a small systematic test on the effect of the material density on the performance metrics before corrections are applied. The same analysis was performed with an aluminium, vanadium and copper cube to bridge the density difference between water and lead. The utilized measurements and density score thresholds used in the reconstruction of these additional materials are given in Tables VIII, IX and X in the Appendix. The variations σ_D and σ_P were computed over the cube positions in the center, as well as at the maximum and minimum of each axis resulting in only 7 measurement positions to reduce the necessary computation time for this study. The density variation shows no clear trend against the material density, but the values for water and Vanadium are visible outliers compared to the other three measurements. However, the position variation shows a dependency against the density of the cube material with a plateau after reaching the density of Vanadium. This observation can be explained by the fact that the majority of secondary particles is produced in the upper volume of the cube resulting in the positional bias. This effect gets enhanced for materials with higher density, as the probability for the production of secondary particles is also rising with the material density. With increasing density the absorption of secondary particles inside the object becomes more significant, counteracting the higher production rate and hence resulting in the plateau seen for the values of σ_P.

TABLE VII
RESULTS OF THE SYSTEMATIC TEST FOR THE WATER, VANADIUM, COPPER AND LEAD CUBE.

	Water	**Aluminium**	**Vanadium**	**Copper**	**Lead**
$\boldsymbol{\sigma_D}$	10.6 %	11.5 %	13.5 %	11.5 %	11.2 %
$\boldsymbol{\sigma_P}$	0.09 m	0.12 m	0.15 m	0.15 m	0.15 m

VI. DISCUSSION

Secondary particles have been proven to be a valuable complementary approach to muon scattering or radiography methods. While this work showed that the bias due to the position of the object can not be neglected, it also provided a proof-of-principle that a correction against this effect is feasible. With the correction of the density score and the reconstructed position for simple cube shapes made out of water or lead, the results from this stand-alone approach are no longer ambiguous due to the geometric location inside the container.

However, the correction method explained and presented in this work needs further generalisation to be applied as a tool for a complete secondary particle reconstruction approach. The corrections show a material dependency, which creates the need for a correction database for a wider range of material densities. Future studies could include a more generalized correction procedure based on machine learning methods to eliminate this problem. Furthermore, the broad binning of the correction map is prone to under- or over-correct within a single bin, especially for bins with large corrections and steeply rising correction factor behavior between adjacent bins. This can only be improved by defining a finer grid of measurement points and enhanced interpolation for the bins in between, potentially based on a fit with a functional form.

Nonetheless, the approach introduced by the authors in previous publications together with the studies presented in this work will lay the foundation for a first combination of stand-alone secondary particle analysis with MST or MR

results. Similar to the work presented in this paper, these results obtained from the muon measurements will also be studied for potential evidence of such geometrical biases, which are expected to be significantly smaller than the results shown in this work though. This will allow for the first time to understand the potential performance enhancement of such a combined approach. Further steps will also include machine learning based enhancements of the analysis through the derivation of improved combination procedures, as well as object detection and classification algorithms.

APPENDIX

TABLE VIII
MEASUREMENTS AND DENSITY SCORE THRESHOLDS USED IN THE RECONSTRUCTION OF THE ALUMINIUM CUBE.

	Photons	Neutrons	Electrons
Upper detector: Production	20 %	–	–
Upper detector: Absorption	–	–	–
Sidewise detector: Production	30 %	–	–
Sidewise detector: Absorption	–	–	–
Lower detector: Production	–	–	–
Lower detector: Absorption	30 %	40 %	40 %

TABLE IX
MEASUREMENTS AND DENSITY SCORE THRESHOLDS USED IN THE RECONSTRUCTION OF THE VANADIUM CUBE.

	Photons	Neutrons	Electrons
Upper detector: Production	25 %	–	–
Upper detector: Absorption	–	–	–
Sidewise detector: Production	30 %	–	–
Sidewise detector: Absorption	–	–	–
Lower detector: Production	–	–	–
Lower detector: Absorption	35 %	40 %	45 %

TABLE X
MEASUREMENTS AND DENSITY SCORE THRESHOLDS USED IN THE RECONSTRUCTION OF THE COPPER CUBE.

	Photons	Neutrons	Electrons
Upper detector: Production	30 %	–	–
Upper detector: Absorption	–	–	–
Sidewise detector: Production	30 %	–	–
Sidewise detector: Absorption	–	–	–
Lower detector: Production	–	–	–
Lower detector: Absorption	35 %	40 %	45 %

REFERENCES

[1] Morishima, K.; Kuno, M.; Nishio, A.; Kitagawa, N.; Manabe, Y.; Moto, M.; Takasaki, F.; Fujii, H.; Satoh, K.; Kodama, H.; et al. Discovery of a big void in Khufu's Pyramid by observation of cosmic-ray muons. *Nature* **2017**, *552*.

[2] Marteau, J.; de Bremond d'Ars, J.; Gibert, D.; Jourde, K.; Ianigro, J.C.; Carlus, B. DIAPHANE: Muon tomography applied to volcanoes, civil engineering, archaelogy. *Journal of Instrumentation* **2017**, *12*.

[3] Borozdin, K.; Greene, S.; Lukić, Z.; Milner, E.; Miyadera, H.; Morris, C.; Perry, J. Cosmic ray radiography of the damaged cores of the Fukushima reactors. *Physical Review Letters* **2012**, *109*.

[4] Clarkson, A.; Ireland, D.G.; Al Jebali, R.; Kaiser, R.; Lumsden, S.; Mahon, D.; Mountford, D.; Ryan, M.; Shearer, C.; Yang, G. Characterising encapsulated nuclear waste using cosmic-ray Muon Tomography (MT). In Proceedings of the 2015 International Conference on Advancements in Nuclear Instrumentation Measurement Methods and Their Applications (ANIMMA), Lisbon, Portugal, 20–24 April 2015.

[5] Tanaka, H.K.; Taira, H.; Uchida, T.; Tanaka, M.; Takeo, M.; Ohminato, T.; Aoki, Y.; Nishitama, R.; Shoji, D.; Tsuiji, H. Three-dimensional computational axial tomography scan of a volcano with cosmic ray muon radiography. *Journal of Geophysical Research: Solid Earth* **2010**, *115*.

[6] Fehr, F. and the TOMUVOL Collaboration. Density imaging of volcanos with atmospheric muons. *Proceedings of the Journal of Physics: Conference Series* **2012**, *375*.

[7] Armitage, J.; Botte, J.; Boudjemline, K.; Erlandson, A.; Robichaud, A.; Bueno, J.; Bryman, D.; Gazit, R.; Hydomako, R.; Liu, Z.; et al. First images from the CRIPT muon tomography system. *Proceedings of the International Journal of Modern Physics: Conference Series* **2014**, *27*.

[8] Barnes, S.; Georgadze, A.; Giammanco, A.; Kiisk, M.; Kudryavstev, V.; Lagrange, M.; Pinto, O.L.; Cosmic-Ray Tomography for Border Security. *Instruments* **2023**, *7*.

[9] Greisen, K. Cosmic ray showers. *Annual Review of Nuclear and Particle Science* **1960**, *10*.

[10] Gaisser, T.K.; Engel, R.; Resconi, E. Cosmic Rays and Particle Physics. Cambridge University Press: Cambridge, UK, 2016.

[11] Heck, D.; Knapp, J.; Capdevielle, J.; Schatz, G.; Thouw, T. CORSIKA: A Monte Carlo code to simulate extensive air showers. Technical Report; FZKA-6019; Karlsruhe Institute of Technology, Karlsruhe, Germany; 1998.

[12] Hagmann, C.; Lange, D.; Wright, D. Cosmic-ray shower generator (CRY) for Monte Carlo transport codes. In Proceedings of the 2007 IEEE Nuclear Science Symposium (NSS), Honolulu, USA, 26 October–3 November 2007; Volume 2.

[13] Schultz, L.J.; Blanpied, G.S.; Borozdin, K.N.; Fraser, A.M.; Hengartner, N.W.; Klimenko, A.V.; Morris, C.L.; Orum, C.; Sossong, M.J. Statistical reconstruction for cosmic ray muon tomography. *IEEE Transactions on Image Processing* **2007**, *16*.

[14] Barnes, S.; Stephan, M.; Sill Torres, F.; Gabriel, A.; Wrede, C.P.; Wendt, N.S.; Nickel, V. The COSMICS (Container Scanning by Muon-based Imaging using Cosmic rayS) Project; an introduction and preliminary results. In Proceedings of the 2021 European Workshop on Maritime Systems Resilience and Security (MARESEC), Virtual, 14 June 2021.

[15] Saracino, G.; Ambrosino, F.; Bonechi, L.; Cimmino, L.; D'Alessandro, R.; D'Errico, M.; Noli, P.; Scognamiglio, L.; Strolin, P. Applications of muon absorption radiography to the fields of archaeology and civil engineering. *Philosophical Transactions of the Royal Society* **2019**, *377*.

[16] Carbone, D.; Gibert, D.; Marteau, J.; Diament, M.; Zuccarello, L.; Galichet, E. An experiment of muon radiography at Mt Etna (Italy). *Geophysical Journal International* **2014**, *196*.

[17] Perkins, D.H. Introduction to High Energy Physics. Cambridge University Press: Cambridge, UK, 2000.

[18] Martin, B.R.; Shaw, G. Particle Physics. John Wiley & Sons: Hoboken, USA, 2017.

[19] Cottingham, W.N.; Greenwood, D.A. An Introduction to Nuclear Physics. Cambridge University Press: Cambridge, UK, 2001.

[20] Blackwell, T.; Kudryavtsev, V. Development of a 3D muon disappearance algorithm for muon scattering tomography. *Journal of Instrumentation* **2015**, *10*.

[21] Particle Data Group; et al. Review of particle physics. *Progress of Theoretical and Experimental Physics* **2022**, *8*.

[22] Ferrari, A.; Sala, P.R. The Physics of High Energy Reactions. Technical Report; CERN-ATL-PHYS-97-113; CERN, Geneva, Switzerland; 1997.

[23] Leo, W.R. Techniques for Nuclear and Particle Physics Experiments: A How-to Approach. Springer Science & Business Media: Berlin/Heidelberg, Germany, 2012.

[24] Stein, P.; Odian, A.; Wattenberg, A.; Weinstein, R. Dependence on atomic number of the nuclear photoeffect at high energies. *Physical Review* **1960**, *119*.

[25] Bikit, I.; Mrdja, D.; Bikit, K.; Slivka, J.; Jovancevic, N.; Oláh, L.; Hamar, G.; Varga, D. Novel approach to imaging by cosmic-ray muons. *Europhysics Letters* **2016**, *113*.

[26] Galgóczi, G.; Mrdja, D.; Bikit, I.; Bikit, K.; Slivka, J.; Hansman, J.; Oláh, L.; Hamar, G.; Varga, D. Imaging by muons and their induced secondary particles—A novel technique. *Journal of Instrumentation* **2020**, *15*.

[27] Bacon, J.D.; Borozdin, K.N.; Fabritius, I.; Joseph, M.; Morris, C.; Perry, J.O. Muon Induced Fission Neutrons in Coincidence with Muon Tomography; Technical Report; LA-UR-13-28292; Los Alamos National Laboratory, Los Alamos, USA; 2013.

[28] Borozdin, K.N.; Morris, C.; Klimenko, A.V.; Spaulding, R.; Bacon, J. Passive imaging of SNM with cosmic-ray generated neutrons and gamma-rays. In Proceedings of the IEEE Nuclear Science Symposium (NSS), Knoxville, USA, 30 October–6 November 2010.

[29] Luo, S.Y.; Huang, Y.H.; Ji, X.T.; He, L.; Xiao, W.C.; Luo, F.J.; Feng, S.; Xiao, M.; Wang, X.D. Hybrid model for muon tomography and quantitative analysis of image quality. *Nuclear Science and Techniques* **2022**, *33*.

[30] Blackwell, T.B. The Use of Cosmic-Rays in Detecting Illicit Nuclear Materials. Ph.D. Thesis; University of Sheffield, Sheffield, UK; 2015.

[31] Pérez Prada, M.; Barnes, S.; Stephan, M. Analysis of Secondary Particles as a Complement to Muon Scattering Measurements. *Instruments* **2022**, *6*.

[32] Pérez Prada, M.; Barnes, S.; Stephan, M. Stand-alone cosmic-ray tomography with secondary particles. *Journal of Advanced Instrumentation in Science* **2024**, *1*.

[33] Agostinelli, S.; Allison, J.; Amako, K.; Apostolakis, J.; Araujo, H.; Arce, P.; Asai, M.; Axen, D.; Banerjee, S.; Barrand, G.; et al. GEANT4—A simulation toolkit. *Nuclear Instruments and Methods in Physics Research Section A: Accelerators, Spectrometers, Detectors and Associated Equipment* **2003**, *506*.

[34] Koi, T. A Geant4 physics list for shielding calculation. In Proceedings of the Shielding Aspects of Accelerators, Targets and Irradiation Facilities (SATIF), Geneva, Switzerland, 2–4 June 2010.